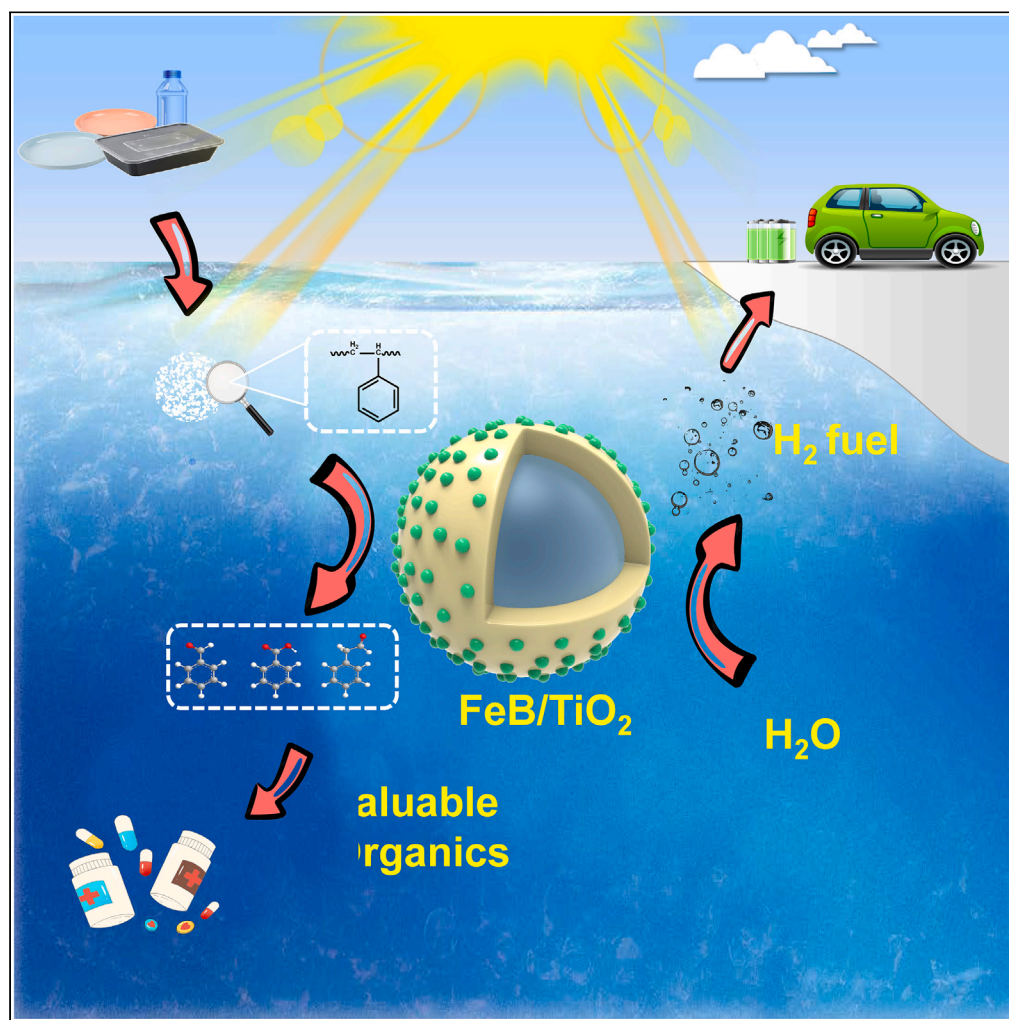Article

Efficient photodegradation of polystyrene microplastics integrated with hydrogen evolution: Uncovering degradation pathways

Jiehong He,
Lanfang Han,
Weiwei Ma, Liying
Chen, Chuanxin
Ma, Chao Xu,
Zhifeng Yang

hanlanfang@gdut.edu.cn

Highlights

FeB/TiO$_2$ exhibited excellent PS MPs degradation and H$_2$ evolution performance

FeB promoted the ROS formation and combination of protons with photoelectrons

Valuable compounds (e.g., benzaldehyde, benzoic acid, etc.) were detected

The route of PS-MPs degradation was revealed and simulated by DFT calculation

CellPress
OPEN ACCESS

Article

Efficient photodegradation of polystyrene microplastics integrated with hydrogen evolution: Uncovering degradation pathways

Jiehong He,[1,2] Lanfang Han,[1,2,4,*] Weiwei Ma,[1] Liying Chen,[1] Chuanxin Ma,[1,2] Chao Xu,[3] and Zhifeng Yang[1,2]

SUMMARY

Photocatalytic microplastics (MPs) conversion into valuable products is a promising approach to alleviate MPs pollution in aquatic environments. Herein, we developed an amorphous alloy/photocatalyst composite (FeB/TiO$_2$) that can successfully convert polystyrene (PS) MPs to clean H$_2$ fuel and valuable organic compounds (92.3% particle size reduction of PS-MPs and 103.5 μmol H$_2$ production in 12 h). FeB effectively enhanced the light-absorption and carrier separation of TiO$_2$, thereby promoting more reactive oxygen species generation (especially $\cdot$OH) and combination of photoelectrons with protons. The main products (e.g., benzaldehyde, benzoic acid, etc.) were identified. Additionally, the dominant PS-MPs photoconversion pathway was elucidated based on density functional theory calculations, by which the significant role of $\cdot$OH was demonstrated in combination with radical quenching data. This study provides a prospective approach to mitigate MPs pollution in aquatic environments and reveals the synergistic mechanism governing the photocatalytic conversion of MPs and generation of H$_2$ fuel.

INTRODUCTION

To meet the high demand for plastic products, plastics are being produced in large quantities. Once being improperly treated, they may form microplastics (MPs) following fragmentation and aging, which cause serious pollution in aquatic environments and even threaten human health.[1–7] It was estimated that 209.7 trillion MPs (306.9 tons) are discharged into aquatic environments in China per year, and more than 80% of them come from the wastewater of sewage treatment plants.[8] Polystyrene (PS) was a rather typical MPs which has been extensively detected in waters,[9] and frequently regarded as the research model of MPs in the studies on MPs biotoxicity.[10,11] So far, numerous studies have shown the detrimental effects PS-MPs on marine ecosystems and human health.[12] It is therefore urgent to develop feasible approaches to mitigate MPs (especially PS-MPs) pollution or transform them into valuable products.

Considering the high stability and anti-oxidation properties of plastics, various technologies have been developed to alleviate MPs pollution, including the manufacture of biodegradable and photodegradable plastics, thermal or catalytic degradation processes, and enzymatic degradation methods.[13–15] Among these approaches, photocatalysis has been widely demonstrated as a green and efficient approach.[16] Titanium dioxide (TiO$_2$) has been used as a photocatalyst applied in pollutant degradation for decades due to its outstanding performance in mitigating water pollution (e.g., organic contaminants, heavy metal, etc.) under mild conditions.[17] Importantly, it contributes to the effective generation of reactive oxygen active species (ROS) under UV light irradiation,[18] which is promising in terms of alleviating MPs pollution.[19] The photocatalytic performance of TiO$_2$ can be reinforced by modulating its crystal phase and structure.[20,21] For example, the anatase crystalline structure promotes significant pollutant degradation owing to its superior $\bullet$OH generation capabilities.[22] Our group previously demonstrated that TiO$_2$ with a core-shell structure was efficient in light harvesting, which facilitated photoelectron-hole separation.[23] However, the fact that TiO$_2$ can only be stimulated by UV light because of the broad forbidden band (3.2 eV) limits its application in photocatalysis.[24] Meanwhile, it is well known that hydrogen (H$_2$) is a valuable product that can be used in agricultural, pharmaceutical, chemical, and renewable energy applications.[25,26] Photocatalytic water splitting using TiO$_2$ represents a promising approach for H$_2$ production; however, it also suffers from high charge carrier recombination and low light absorption.[27,28] Thus, it is crucial to develop a new approach to promote he photocatalytic efficiency of TiO$_2$. Noble metal loading can accelerate the

[1]Key Laboratory for City Cluster Environmental Safety and Green Development of the Ministry of Education, School of Ecology, Environment and Resources, Guangdong University of Technology, Guangzhou 510006, China

[2]Southern Marine Science and Engineering Guangdong Laboratory (Guangzhou), Guangzhou 511458, China

[3]Research Center for Eco-Environmental Engineering, Dongguan University of Technology, Dongguan 523808, China

[4]Lead contact

*Correspondence:
hanlanfang@gdut.edu.cn

https://doi.org/10.1016/j.isci.2023.106833

separation and migration of photogenerated charge carriers.[29–31] However, the scarcity and high costs of noble metals hinder their industrial applications. Recently, transition metal borides have garnered attention in photocatalytic H_2 evolution reaction (HER) owing to their unique coordination environments and electronic structures.[32–34] Among numerous transition metals, the iron (Fe)-based catalyst has deserved particular attention due to their high natural abundance.[35] In addition, due to the sufficient valence states of iron, the electronic property could be regulated for supporting multiple reactions.[36] Particularly, Fe group borides were proved to have excellent HER activity owing to better electron transfer kinetics from boron to metal, in which the d-orbitals are filled by the electrons from boron, boosting the intrinsic catalytic activity of Fe.[37,38] Moreover, combining transition metal borides (e.g., FeB) with TiO_2 can improve the capacity of light harvesting and charge separation. This facilitates the oxidation of substrates (e.g., MPs, organic pollutants) to other organic compounds while photoelectrons could reduce the protons to H_2.[39,40] In addition, previous studies rarely investigated the reaction pathway(s) involved in photocatalytic MPs degradation. Analyzing the intermediates produced during the reaction and investigating the catalyst structure are expected to provide an in-depth understanding of the photocatalytic MPs degradation mechanism.

In this work, a transition metal (Fe) boride/photocatalyst composite (i.e., FeB/TiO$_2$) was synthesized and applied for photocatalytic PS-MPs conversion and water splitting. The structural and electronic properties were characterized, and the mechanisms of MPs degradation and synergetic H_2 evolution were explored. Analysis of the ROS generation, detection of intermediates, and density functional theory (DFT) calculations revealed the reaction pathways related to MPs degradation. This work provides a new approach for developing photocatalysts that exhibit enhanced MPs degradation and water-splitting activities and contributes new insights into the reaction mechanism governing the photo-transformation of MPs.

RESULTS AND DISCUSSION

Structural and photoelectrochemical characterization

The core-shell structure TiO_2 (CST) was synthesized through the alcoholysis method. The FeB-modified TiO$_2$ (FBT) was constructed by the reduction of iron sulfate using NaBH$_4$. Prior to reduction, Fe was loaded onto the surface of TiO$_2$, and the combination with TiO$_2$ was strengthened by low-temperature roasting. During the reduction of Fe ions by BH$_4^-$, a large amount of heat was released. Ice water was applied to reduce the reaction temperature, limiting the FeB agglomeration on the surface of TiO$_2$ (see the Experimental Procedures section for details). The structure and crystalline phase of all the samples were explored with X-ray diffraction (XRD) (Figure 1A). CST was consistent with the anatase phase based on the peaks at 25.3°, 37.8°, and 48.0°, corresponding to the (101), (004), and (200) crystalline planes, respectively. FeB had an apparent peak at ~45°; however, no Fe peak was observed in FeB/TiO$_2$ composites with low Fe content (e.g., 3FBT and 5FBT). This result was attributed to (1) the dispersion of Fe on the surface of CST and (2) high crystallinity of TiO$_2$, which might mask the characteristic peak of FeB with an amorphous structure. As the Fe content increased (e.g., 7FBT and 9FBT), the characteristic peak of FeB (at ~45°) gradually grew from the enlarged pattern of XRD (Figure S2A), whereas the CST peaks showed almost no change, indicating that FeB modification did not appreciably affect the structure of CST. This result was supported by the SEM images (Figures 1B–1E). The CST and FeB/TiO$_2$ composites all adopted core-shell structures with particle sizes ranging between 2 and 3 μm, consistent with the transmission electron microscope (TEM) images (Figures 1F–1H). Moreover, TiO$_2$ displayed a distinct anatase crystal structure with a lattice spacing of 0.35 nm, corresponding to the (101) crystal plane, as also demonstrated in the XRD pattern. The elemental distribution of FeB/TiO$_2$ further revealed the existence of FeB and TiO$_2$, where FeB nanoparticles (~10 nm in diameter) were uniformly dispersed on the surface of CST (Figure 1I).

The Fe contents of all samples were determined, and all cases were close to the theoretical contents (Table S1). The specific surface area (S$_{BET}$) and pore structures were analyzed based on the BJH model (Figures S2B and S2C and Table S2). The profiles of all the samples showed H3 hysteresis loops, indicating abundant mesoporous structures. Compared with CST, the S$_{BET}$ of FeB/TiO$_2$ composites decreased. In addition, the pore volume and pore size decreased with increasing Fe content, which was ascribed to the smaller FeB particles on the surface of CST entering the pore channels.

The surface electronic structures of the catalysts were investigated by X-ray photoelectron spectroscopy, which was calibrated with the binding energy of polluted carbon (at 284.8 eV). As shown in Figure 2A, all Ti species in CST were in the Ti^{4+} state, with corresponding binding energies at 458.6 and 464.3 eV.[41] The
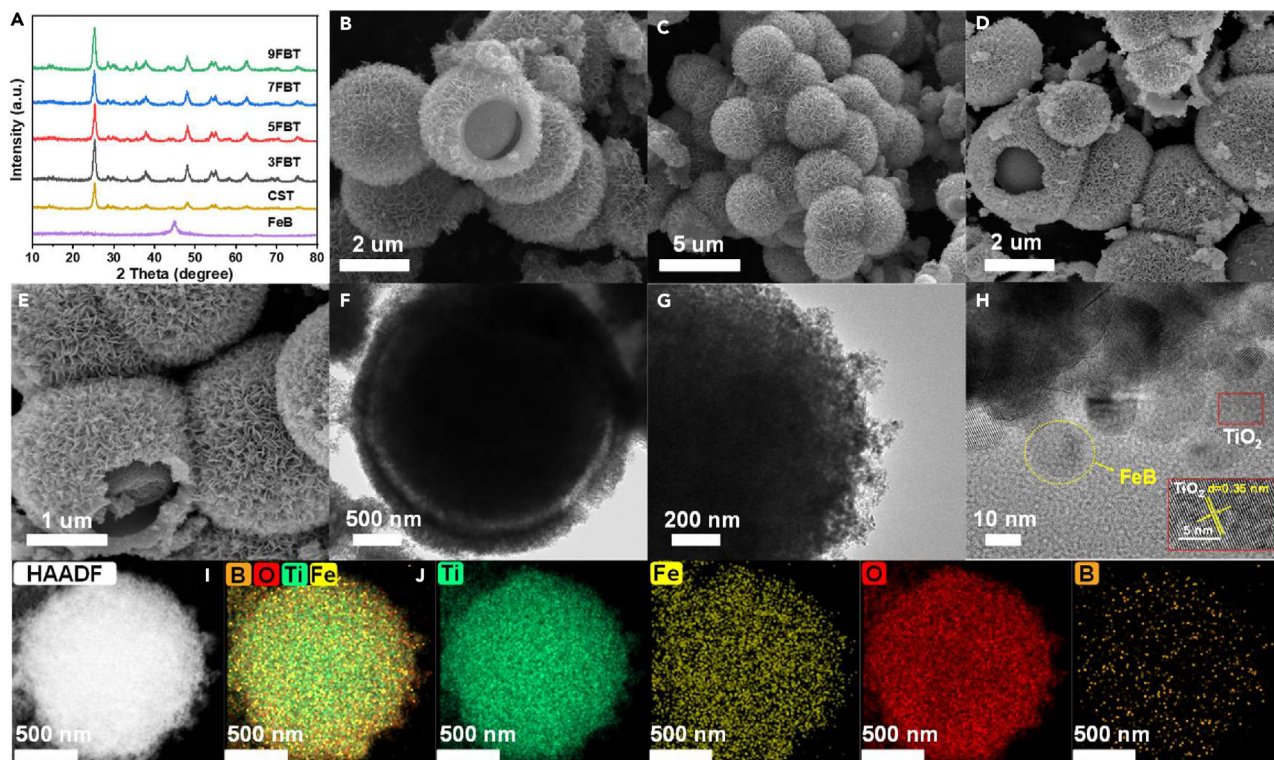
Figure 1. Structural characterization of samples
(A) X-ray diffraction (XRD) patterns of CST, FeB, and xFBT.
(B–E) Scanning electron microscope (SEM) images of CST (B and C) and 7FBT (D and E).
(F–I) Transmission electron microscopy (TEM) images of 7FBT with different scales.
(J) Elemental mapping images of 7FBT.
Note that CST, FeB, 7FBT were short for core-shell structured TiO_2, iron boron amorphous alloy, FeB/TiO_2 composites with 7 % theoretical mass ratio of Fe, respectively.

peaks associated with the FeB/TiO_2 composite (i.e., 7FBT) were shifted toward higher energy compared with those in CST, indicating that the Ti species in the FeB/TiO_2 composite were at a relatively electron-deficient state. Meanwhile, the peaks at 529.6 and 531.6 eV in the O 1s spectra of CST and 7FBT were assigned to the Ti–O bonds and surface hydroxyl (–OH) groups, respectively (Figure 2B).[42] In the Fe 2p spectra (Figure 2C), FeB and 7FBT both displayed the characteristic doublet corresponding to Fe 2p1/2 and Fe 2p3/2 at binding energies of approximately 725 and 711 eV, respectively.[43] The binding energy of 7FBT shifted toward lower energy relative to that of FeB. This result suggested that Fe was at an electron-rich state, indicating the formation of Fe species, such as Fe^{2+} and metallic Fe.[43] In addition, the B 1s spectrum of FeB revealed two peaks at approximately 192 and 187.9 eV, corresponding to the boron oxide and alloying states, respectively (Figure 2D).[44] The binding energy of B in 7FBT shifted toward higher energy, implying electron-deficient B sites. Thus, the electrons at the Fe site in FeB/TiO_2 composite could be derived from TiO_2 or B, whereas the electrons from TiO_2 could be transferred to Fe with the Ti–O–Fe bond serving as a bridge. These observations highlighted the high degree of interaction between CST and FeB in 7FBT.

The optical absorption properties of all catalysts were investigated by UV-vis diffuse reflection spectra (UV-vis DRS), and the band gap energy of TiO_2 with or without FeB modification, as well as the cutoff wavelength, were calculated according to Tauc plot (Figure 3B and Table S3). As shown in Figure 3A, all FeB-modified TiO_2 samples displayed enhanced light absorption relative to CST. FeB exhibited a full-wavelength absorption spectrum since FeB was black after reduction by $NaBH_4$ (Figure S3). As the FeB content increased, the absorption edge evolved a red-shifted feature, indicating the beneficial light-harvesting effect of FeB on TiO_2, especially under visible light. In addition, the band gap energies of all FeB-modified TiO_2 samples, especially 7FBT (2.63 eV), were significantly lower than that of CST
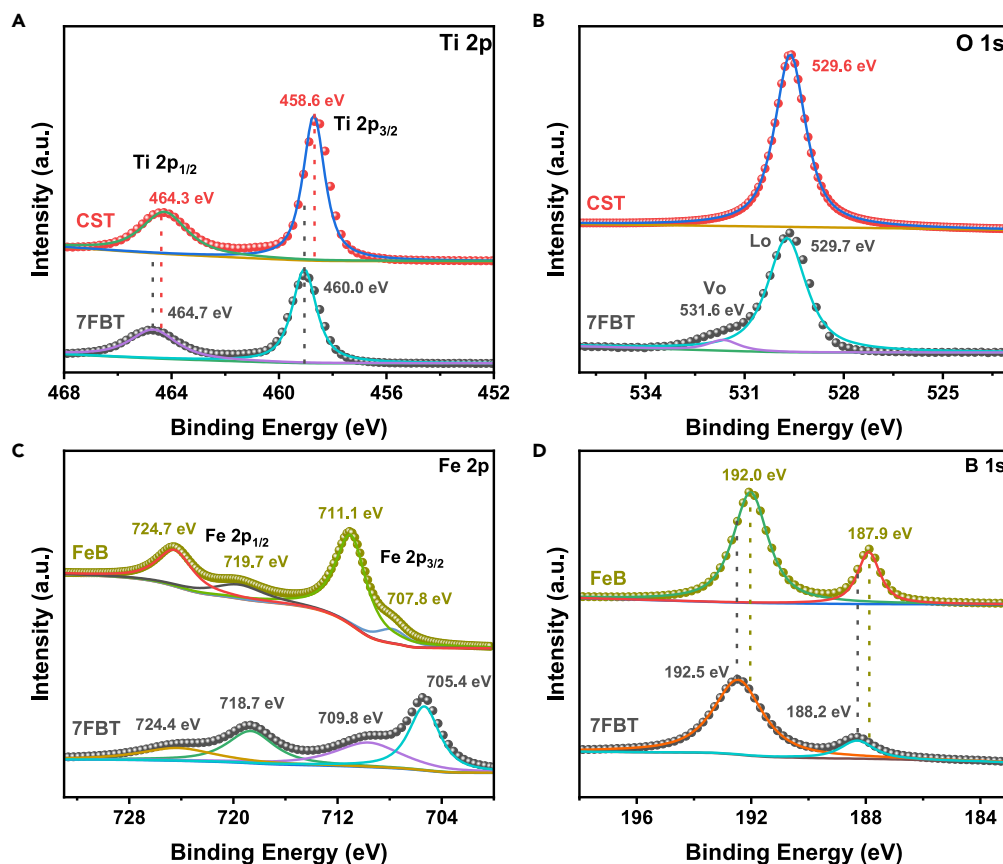
Figure 2. X-ray photoelectron spectroscopy (XPS) spectra of samples
(A–D) XPS spectra for the (A) Ti 2p, (B) O 1s, (C) Fe 2p, and (D) B 1s levels of CST, FeB, and 7FBT.
Note that CST, FeB, 7FBT were short for core-shell structured TiO2, iron boron amorphous alloy, FeB/TiO2 composites with 7 % theoretical mass ratio of Fe, respectively.

(3.21 eV), implying that the light absorption and band structure of CST were finely engineered by the modification of FeB. Meanwhile, it was found a stronger light absorption and wider absorption edge on 7FBT than 7FBT-Commercial without core-shell structure (Figure S3). The forbidden bandwidth of 7FBT (2.63 eV) was significantly lower than that of 7FBT-Commercial (3.0 eV), indicating the stronger light absorption of core-shell structure, leading to the enhanced potential for electron-hole separation.

The steady-state fluorescence spectra were applied to explore the recombination of charge carriers at an excitation wavelength of 350 nm. As shown in Figure 3C, the main peak at 436 nm was ascribed to self-trapped excitons, which originated from the interactions of conduction band electrons localized on Ti 3d orbital with holes present in O 2p. The shoulder peak at 457 nm was attributed to the defect centers trapping electrons (e.g., oxygen vacancy).[45] Reduced peak intensity was observed in all FeB/TiO2 composites, indicating lower carrier recombination. As the proportion of FeB increased, the rate of carrier recombination tended to decrease, reaching its lowest value in 7FBT. This was consistent with a greater photoelectron-hole separation following the modification with FeB. However, a further increase in FeB content (i.e., 9FBT) reduced the carrier separation. This result was attributed to the fact that light absorption was hindered by the excess FeB on the CST surface. Overall, these results demonstrated the regulation effect of FeB content on the carrier separation of FeB/TiO2 composites.

Figure 3D presents the photocurrent response spectra of samples obtained following irradiation by a 300 W Xe lamp. Compared with CST, the FeB/TiO2 composites were expected to exhibit enhanced photocurrents as the FeB content increased (from 3FBT to 7FBT), corresponding to the increased electron density. This was expected because of the superior light-harvesting capabilities and photoelectron-hole
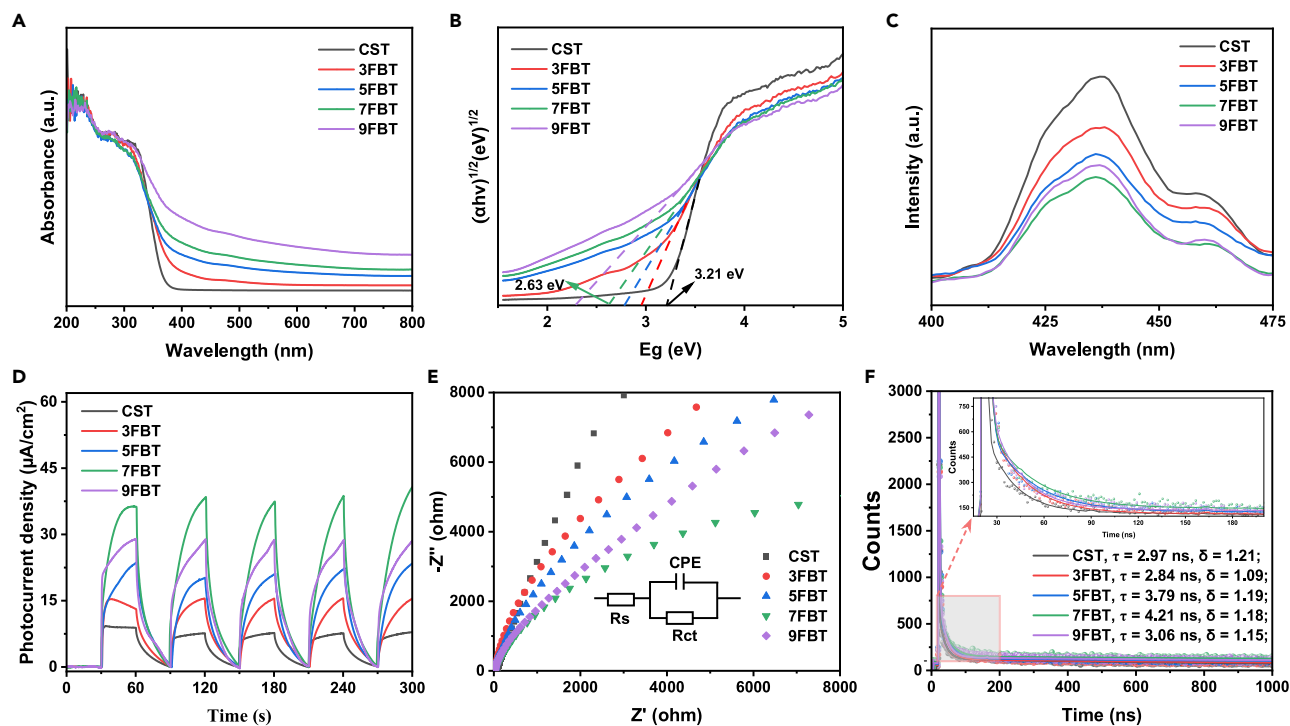
Figure 3. Photoelectrochemical characterization of samples

(A and B) UV-vis diffuse reflection spectra (UV-vis DRS) (A) and the corresponding plots of (αhν)1/2 as a function of hν (B).

(C) Steady-state fluorescence spectra at an excitation wavelength of 350 nm.

(D) Photocurrent response spectra under irradiation by a 300 W Xe lamp.

(E) Electrochemical impedance analysis with the equivalent circuit diagram in the inset. CPE: constant phase element; Rs: diffusion electric resistance; Rct: charge transfer resistance.

(F) Luminescence decay curves with the enlarged patterns in the inset (excitation wavelength = 350 nm). τ: the average lifetime.

separation (*vide supra*). However, the excess FeB on the surface resulted in lower photocurrent owing to the shading effect of the excess FeB on CST. In addition, the electrochemistry impedance of all samples was measured by electrochemical impedance spectra. All samples displayed one dominant semicircle, whose diameter is related to charge-transfer resistance.[46] As displayed in Figure 3E, 7FBT exhibited a smaller arc radius than other samples, indicating a smaller charge-transfer resistance and faster photogenerated charge transfer kinetics.

To determine the lifetime of the charge carriers in TiO_2 and FeB-modified TiO_2 samples, fluorescence emission decay was studied with the excitation wavelength of 350 nm (Figure 3F). As shown in the enlarged plots (inset of Figure 3F), all FeB-modified TiO_2 revealed a longer fluorescence lifetime compared to pure TiO_2. This can be accounted by slower electron-hole recombination.[47] A suitable increase in Fe content could prolong the charge carrier lifetime. In particular, 7FBT exhibited the longest lifetime (τ = 4.21 ns), which was 1.42 times higher than CST (τ = 2.97 ns). However, excessive FeB could become the sites of electron-hole recombination, leading to a shorter lifetime. Therefore, moderate FeB-modification can prolong the fluorescence lifetime, which endows photogenerated charge carriers with sufficient time to migrate the catalyst surface to participate in the reaction.

Photocatalytic PS-MPs degradation synergistic H_2 evolution

The particle size reduction of PS-MPs during the reaction was an important indicator of degradation efficiency.[48] As shown in Figure 4A, pure photolysis led to a slight reduction in particle size (10% after 12 h). However, the particle size decreased considerably after the addition of a photocatalyst, and FeB/TiO_2 composites exhibited enhanced activity in terms of particle size reduction compared with pure CST or FeB. Moreover, this activity was correlated with the FeB content. As the FeB content increased (from 3FBT to 7FBT), the average extent of particle size reduction after 12 h increased from 72.9% to 92.3%. In
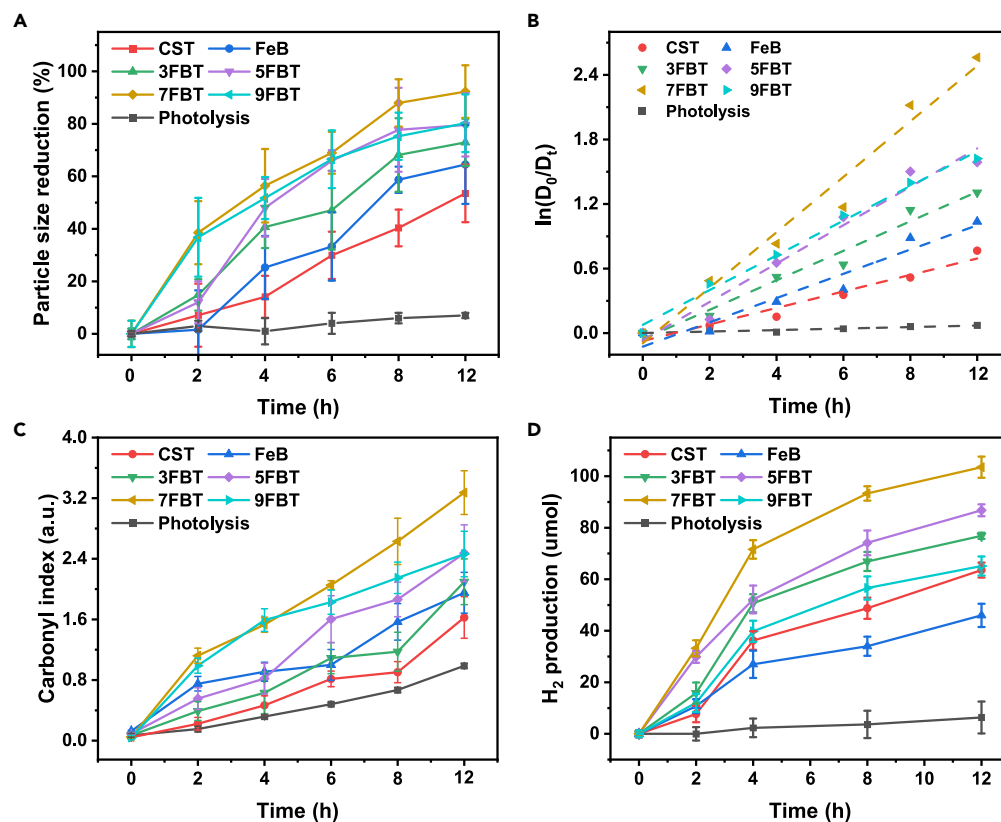
Figure 4. The performance of photocatalytic polystyrene microplastics (PS-MPs) degradation synergetic H$_2$ production

(A and B) Average particle size reduction (A) and corresponding $\ln(D_0/D_t)$-time plot (B) on FeB, CST, and xFBT.

(C and D) Carbonyl index (C) and H$_2$ production (D) on FeB, CST, and xFBT.

Note that "D_0" and "D_t" presented the average diameter of the original and degraded MPs particles during the photocatalytic reaction. CST, FeB, xFBT were short for core-shell structured TiO$_2$, iron boron amorphous alloy, FeB/TiO$_2$ composites with x % theoretical mass ratio of Fe, respectively. Data are represented as mean $\pm$ SEM.

particular, the size reduction achieved by 7FBT increased by 1.72 and 1.43 times compared with CST and FeB, respectively, and 7.29 times relative to pure photolysis. The enhanced photocatalytic performance observed with FeB/TiO$_2$ composites can be partly explained by the increased light absorption enabled by FeB, which accelerated photoelectron-hole separation and migration, thereby generating more ROS for MPs degradation. However, excess FeB (i.e., 9FBT) led to a gradual fall in the size reduction activity. In this case, the limited light absorption caused by the excess FeB on the surface of TiO$_2$ reduced the photochemical activity. A similar activity was observed in the first 6 h due to the saturated active sites provided by FeB. It was further evidenced by the declined activity for continuous increase in FeB content (11FBT in Figure S4A). The core-shell structure of TiO$_2$ also played an important role in PS-MPs photodegradation. Under the same conditions, when replacing TiO$_2$ of core-shell structure in 7FBT with commercial TiO$_2$, the particle size reduction was less (92.3%–43.6% in 12 h) (Figure S5A). Meanwhile, the photocurrent of 7FBT was significantly better than that of 7FBT-Commercial (Figure S5B), indicating a stronger photo-generated electron density. The smaller electrochemical impedance of 7FBT also demonstrated the faster migration of the charge carrier (Figure S5C). Combined with the above UV-vis analysis, it was shown that the core-shell structure of 7FBT can enhance the light absorption and accelerate the carrier separation and migration, thereby leading to a superior photocatalytic PS-MPs degradation. To quantify the kinetics of the size reduction process, a pseudo-first-order model was applied (Figure 4B). The reaction constants (k) and corresponding correlation coefficients (R^2) were calculated from Figure 4A, and the results are presented in Table S4. The photocatalytic reaction constants (e.g., k = 0.258 in 7FBT) were significantly higher than those obtained with pure photolysis (0.007), indicating accelerated degradation efficiency. The reaction constants of the FeB/TiO$_2$ complexes were higher than those of CST and FeB, as expected,

thus confirming that the enhanced PS-MPs degradation activity was related to the chemical and physical characteristics of FeB/TiO$_2$.

To investigate the modulating effect of temperature on the PS-MPs degradation, the degradation of PS-MPs was carried out without temperature control or under different temperatures (Figure S6). It was found that the degradation efficiency of PS-MPs without temperature control was almost the same as that at 25°C, which was due to the room temperature being close to 25°C. The high temperature (35°C) would lead to a stronger degradation efficiency (95.1% in 12 h), while the low temperature (15°C) had a lower degradation efficiency (79.9% in 12 h), indicating that the PS-MPs degradation was positively correlated with temperature.

In addition to the particle size reduction, MPs degradation was accompanied by surface changes, such as variations in the oxygen-containing functional groups on the surface.[49] The PS-MPs turned yellow after degradation on 7FBT (Figure S7), suggesting the occurrence of photooxidation.[50] Therefore, to further investigate the altered surface properties of PS-MPs during degradation, the functional groups on the PS-MPs surfaces were examined by Fourier transform infrared spectroscopy (Figure S8). Pristine PS-MPs had prominent bands at 2851, 1600, 1452, 756, and 698 cm^{-1}. The peaks at 756 and 698 cm^{-1} were assigned to C–H out-of-plane bending vibrations of the benzene rings.[51] The band at 1600 cm^{-1} corresponded to the C=C bond in vinyl groups, while the band at 1452 cm^{-1} originated from the deformation and skeleton vibration motions of the benzene rings.[52] In contrast, all degraded PS-MPs contained intense C=O bands at 1728 cm^{-1}, indicating the formation of more oxygen-containing groups.[53] Meanwhile, the intensities of the C=C and C–H bands decreased as the reaction time increased, implying the chain secession of PS-MPs.[54] The carbonyl index (CI), which is a crucial parameter that is commonly used to evaluate MPs degradation,[55] was determined from the ratio of the C=O band at 1728 cm^{-1} to the symmetric stretching band of CH$_2$ at 2851 cm^{-1}.[56] As shown in Figure 4C, the CI values of all samples increased steadily as the irradiation time increased and were higher than that of pure photolysis at each time point. In particular, the CI value for 7FBT (3.27) was 3.33 times higher than that of pure photolysis (0.98) after 12 h of irradiation. The CI variation among the tested samples was consistent with the particle size reduction results discussed above, thus further supporting the enhanced oxidation effect of FeB/TiO$_2$ on PS-MPs.

During the photocatalytic PS-MPs degradation process, H$_2$ was released. As shown in Figure 4D, the FeB/TiO$_2$ exhibited higher H$_2$ evolution than CST and FeB. Overall, 7FBT achieved the greatest extent of H$_2$ formation (103.5 μmol) after 12 h of irradiation, which was 1.63 and 2.25 times higher than that of CST (63.5 μmol) and FeB (45.9 μmol), respectively. However, negligible H$_2$ was evolved following pure photolysis, which indicated that FeB/TiO$_2$ can not only facilitate PS-MPs degradation but also accelerate the binding of photogenerated electrons to protons during the reaction, thus leading to effective H$_2$ production. Considering that (i) amorphous alloys have demonstrated the potential for H$_2$ evolution[57] and (ii) H$_2$ production by various FeB/TiO$_2$ samples remained generally consistent with the trend in PS-MPs particle size reduction, it was reasonable to speculate that PS-MPs degradation and H$_2$ production may occur simultaneously during the reaction.

Catalyst stability

Stability is an important indicator to evaluate the quality of catalysts. As shown in Figure S9, both CST and 7FBT maintained good stability after 5 cycles. However, FeB exhibited a slight decrease in activity at the later stages. XRD pattern showed the obvious crystallized peaks of Fe$_2$O$_3$ (e.g., 2 Theta = 35.5° assigned to (110)), and TEM image of FeB after reaction displayed obvious lattice fringe (Figures S10A and B). Therefore, it was inferred that FeB could be oxidized and crystallized during the reaction, resulting in decreased activity. Interestingly, the structure and morphology of CST and 7FBT remained almost unchanged after the reaction (Figures S10C–S10D), indicating the superior stability of CST with core-shell structure. In addition, the electrons generated by TiO$_2$ under irradiation may stabilize FeB and avoid its oxidation, which was demonstrated in our previous study.[58] In general, FeB/TiO$_2$ composite could not only maintain good structural stability but also avoid FeB oxidation during the reaction.

ROS identification and mechanistic insights

ROS generation during photocatalysis has played a crucial role in the degradation of pollutants in water environments.[59] Thus, ROS quenching experiments were performed to evaluate the contributions of various radicals in the reaction. As shown in Figure 5A, the particle size reduction activity decreased by
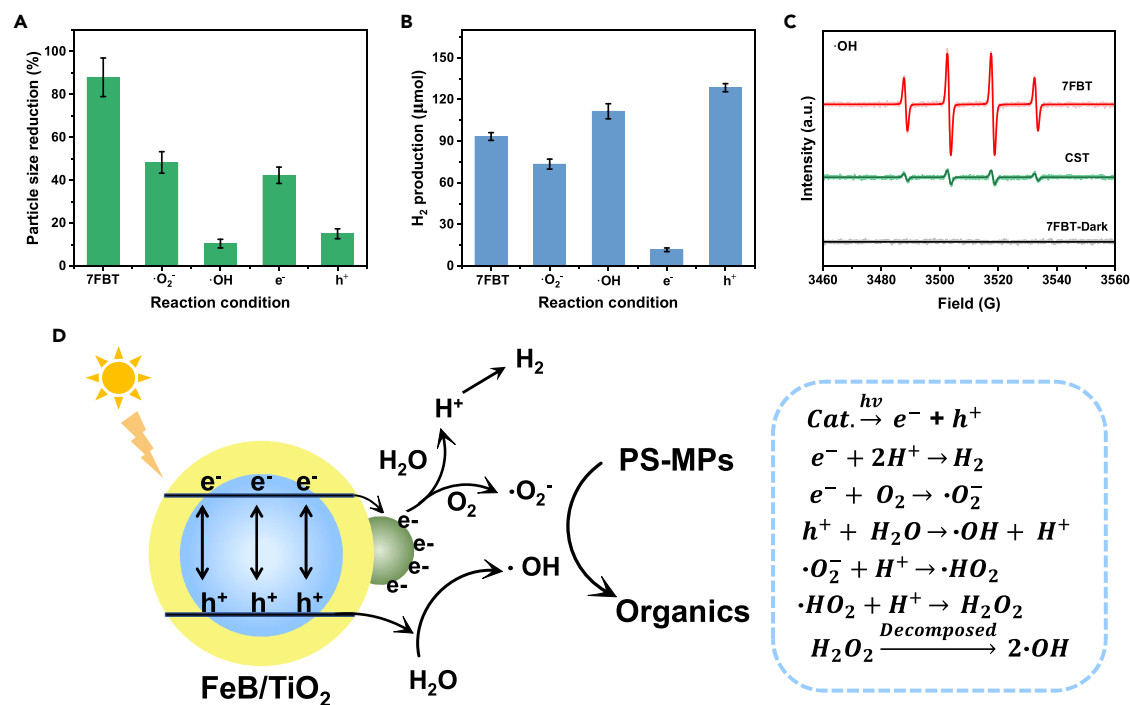
Figure 5. Reactive oxygen species identification and mechanism investigation

(A and B) Average particle size reduction (A) and H_2 production (B) on 7FBT under different conditions.

(C) Electron paramagnetic resonance (EPR) spectrum of $\cdot OH$.

(D) Plausible mechanism for the photocatalytic polystyrene microplastics (PS-MPs) degradation synergetic H_2 evolution.

Note that CST, FeB, 7FBT were short for core-shell structured TiO_2, iron boron amorphous alloy, FeB/TiO_2 composites with 7 % theoretical mass ratio of Fe, respectively. Data are represented as mean $\pm$ SEM.

45.1%, 51.8%, and 82.9% after quenching $\cdot O_2^-$, electrons, and holes, respectively. In particular, the activity was decreased by 88.1% after the quenching of $\cdot OH$, thus highlighting the key role of $\cdot OH$ in the reaction. It is well known that the $\cdot OH$ species are derived from the oxidation of water by photogenerated holes and from the multi-step reaction between photogenerated electrons and $\cdot O_2^-$.[60] The multi-step reactions were initiated by e^- reacting with O_2 to produce $\cdot O_2^-$, which combines with H^+ to generate $\cdot HO_2^-$. In addition, H_2O_2 production followed by dissociation into $\cdot OH$.[61] In this reaction, the presence of FeB promoted sufficient protons generation for the conversion of $\cdot O_2^-$ to $\cdot OH$. Meanwhile, the reduced PS-MPs degradation was appreciable after quenching of $\cdot O_2^-$ and electrons, implying that both $\cdot O_2^-$ and electrons were involved in the degradation reaction. However, the H_2 evolution conditions were different. Figure 5B shows a slight enhancement in H_2 production after quenching holes, which was due to the reinforced separation of photogenerated charge carriers after quenching the holes. This led to more electrons interacting with the protons. Interestingly, H_2 production was hindered slightly after quenching the $\cdot O_2^-$. This could likely be attributed to the fact that $\cdot O_2^-$ quenching promoted the reaction between electrons and oxygen, i.e., more electrons were directed toward $\cdot O_2^-$ generation rather than proton reduction, thereby slightly decreasing H_2 production. The slight increase in H_2 production after quenching $\cdot OH$ was ascribed to the fact that $\cdot OH$ consumption could cause the water oxidation ($H_2O + h^+ \rightarrow \cdot OH + H^+$) in the positive direction, resulting in more holes production for water oxidation. Meanwhile, more photoelectrons separated will combine with protons, leading to more H_2 generation. The reduced activity after quenching electrons further indicated that photoelectrons from 7FBT will react with protons to generate H_2. Electron paramagnetic resonance (EPR) spectroscopy was used to further confirm the ROS contributing to the reaction. As shown in Figure 5C, no signal was observed under dark conditions. Under irradiation, the signal corresponding to $\cdot OH$ in the 7FBT reaction was significantly stronger than that in the reaction with CST, whereas the intensity of the $\cdot O_2^-$ peak in the 7FBT reaction increased only slightly (Figure S4B). These results indicated a stronger promoting effect on $\cdot OH$ generation than $\cdot O_2^-$ generation by FeB/TiO_2 under light irradiation. As reported in previous studies, $\cdot OH$ may originate from two processes: water oxidation or $\cdot O_2^-$ conversion.[62,63] Hence, it was inferred that although FeB on the surface of CST promoted

Table 1. Gas chromatography-mass spectrometer analysis of the liquid reaction products

Samples	Products
7FBT-4 h	Toluene, styrene, and α-methyl styrene
7FBT-12 h	Benzaldehyde, phenylacetaldehyde, and benzoic acid

The different reaction times for 7FBT were donated as 7FBT-y h, where y represented the reaction time.

the reaction between photoelectrons and oxygen to generate $\cdot O_2^-$, some of the $\cdot O_2^-$ was converted into $\cdot OH$. In addition, ROS generation in the reaction was confirmed by the control experiment (Figure S11). Light irradiation and the chemical combination of CST with FeB were the key factors. Under dark condition or mechanically mixing FeB with CST in equal proportions of 7FBT, the corresponding degradation activity (expressed by particle size reduction and CI index) was significantly inhibited in comparison with 7FBT (Figures S8I and S11).

To gain insight into the capacity of •OH generation on different FeB/TiO$_2$ composite, the concentrations of •OH ([•OH]) were determined by terephthalic acid probe method (Figure S12).[64] FeB was found to significantly enhance the •OH generation of TiO$_2$, and [•OH] reached the highest value at 7FBT (8.31 μM in 50 min), which was 3.26 times higher than that of CST (2.55 μM in 50 min) under the same conditions (Table S5). These results illustrated that (1) FeB can effectively enhance the capacity of the •OH generation on CST, and (2) FeB loading can have a modulating effect on the •OH concentration, thus enhancing the PS-MPs degradation.

By analyzing the ROS generation and resolving the band structure of the FeB/TiO$_2$ composite, a possible mechanism for the photocatalytic PS-MPs degradation synergistic H$_2$ evolution reaction could be established. As shown in Figure 5D, the FeB/TiO$_2$ complex was stimulated under light irradiation, resulting in greater photogenerated electron-hole separation. The holes oxidized water to generate $\cdot OH$, while photogenerated electrons from the composite could bind protons to produce H$_2$ or interact with O$_2$ to form $\cdot O_2^-$. The $\cdot O_2^-$ then combined with protons to form $\cdot HO_2^-$, which went on to produce H$_2$O$_2$. Then, H$_2$O$_2$ decomposed to give $\cdot OH$.[62,63] Overall, the ROS generated in the reaction ($\cdot O_2^-$ and $\cdot OH$) could support PS-MPs degradation. Meanwhile, photoelectrons reacted with protons to generate H$_2$, and FeB on the surface of CST accelerated ROS generation (especially $\cdot OH$) and H$_2$ production.

The route of PS-MPs degradation and DFT calculations

To further deduce the PS-MPs degradation pathway, the liquid products were extracted after various reaction durations and measured by gas chromatography-mass spectrometry (GCMS). The results were qualitatively resolved by comparing against the extracted ion chromatography of the products in the National Institute of Standards and Technology database. The total ion chromatographs and comparison results are shown in Figures S13A and S14. The main products formed during PS-MPs degradation were toluene, styrene, and α-methyl styrene, which were generated following chain cleavage and rearrangement during the reaction (Table 1),[65] and the reaction pathways were provided in Figure S15. As the reaction continued, oxygen-containing compounds, such as benzaldehyde, phenylacetaldehyde, and benzoic acid were detected, consistent with a photooxidation reaction, as demonstrated in previous studies.[66] Notably, the organic compounds generated during PS-MPs degradation are valuable for practical applications. For example, benzoic acid can be used as an intermediate in the production of benzoates and phthalates,[67] and phenylacetaldehyde is widely used in perfumes owing to its aroma-enhancing properties.[68] Further exploration of the mineralization of PS-MPs revealed that the CO$_2$ content in the gaseous product gradually increased as the reaction time was prolonged (Figure S13B). The rapid accumulation of CO$_2$ at the early reaction stage might be ascribed to the mineralization of the unstable intermediates from chain scission, and the smooth trend in the later period might be attributed to the formation of the stable oxidation products (e.g., benzaldehyde, phenylacetaldehyde, and benzoic acid evidenced by GCMS). This indicated that PS-MPs degradation might follow a pathway involving decomposition-oxidation-mineralization.

Considering that the polymer decomposition process includes chain initiation, propagation, and termination, the findings presented above suggested that ROS (especially $\cdot OH$) can contribute to PS-MPs oxidation and mineralization, and in combination with the GCMS analysis of the intermediates and
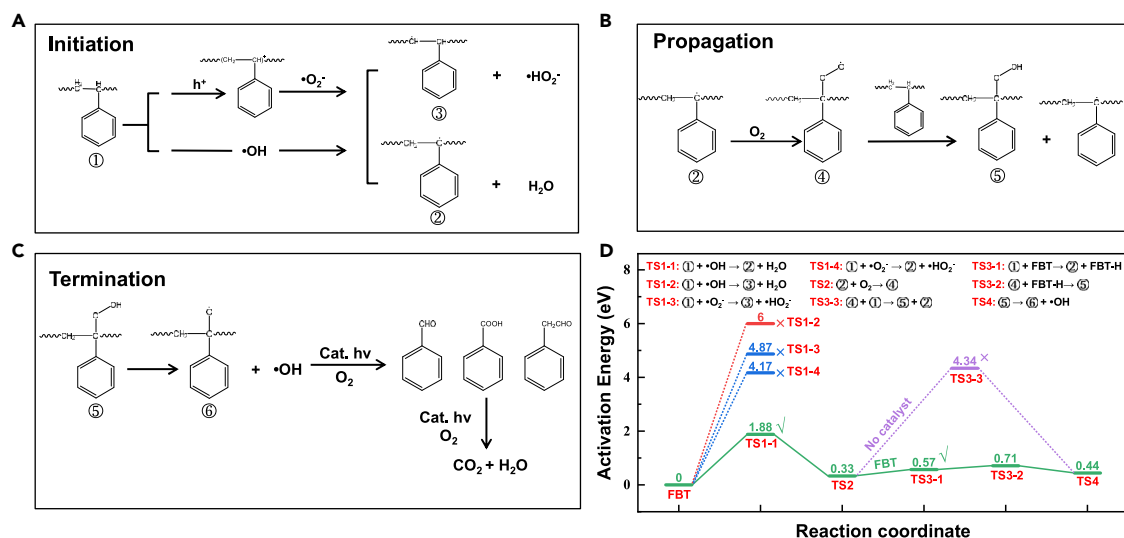
Figure 6. Reaction pathways and related theoretical calculations
(A–C) The pathway of photocatalytic polystyrene microplastics (PS-MPs) degradation including chain initiation (A), propagation (B), and termination (C).
(D) Potential energy diagram from density functional theory (DFT) calculations of PS-MPs degradation.
Note that TS is short for transition state.

products, a possible PS-MPs degradation pathway was proposed. As shown in Figure 6A, during the chain initiation process, $^{•}OH$ and $^{•}O_2^{-}$ can abstract the hydrogen from an α/β carbon connected with the benzene ring of PS molecules, leading to the formation of intermediates 2 and 3. However, it was unclear which intermediates were more readily produced. This dictated the subsequent chain propagation and termination steps. DFT calculations revealed that the activation energies associated with the formation of intermediate 2 (1.88 and 4.17 eV for the $^{•}OH$ and $^{•}O_2^{-}$ dominated pathways, respectively) were significantly lower than those of intermediate 3 (6 and 4.7 eV for the $^{•}OH$ and $^{•}O_2^{-}$ dominated pathways, respectively) (Figure 6D and original data in the Supplemental Information). These calculations indicated that the α-C connection in the benzene ring of PS molecules was vulnerable to be activated and dissociate H, thereby forming intermediate 2. This was particularly evident in the presence of $^{•}OH$, thus confirming the dominant role of $^{•}OH$ in the chain initiation reaction, consistent with the EPR and radical quenching results. During the chain propagation step (Figure 6B), intermediate 2 could integrate oxygen to form intermediate 4 (Transition state (TS) 2, 0.33 eV), and then abstract the hydrogen of another PS molecule. However, the hydrogen abstraction from another PS molecule by intermediate 4 has an extremely high barrier (TS3-3, 4.34 eV). Interestingly, after the addition of FeB/TiO_2, this process was split into two steps, each with low activation energies: first, the H from another PS molecule was abstracted by FeB/TiO_2 to form intermediate 2 (TS3-1, 0.57 eV), and then the H on the surface of FeB/TiO_2 combined with intermediate 4 to form intermediate 5 (TS3-2, 0.71 eV), triggering the rapid onset of the chain propagation reaction. Next, a hydroxyl group was abstracted from intermediate 5 to produce intermediate 6 (TS4, 0.44 eV), thereby ultimately forming benzaldehyde, phenylacetaldehyde, and benzoic acid via photocatalytic oxidation (Figure 6C).

Conclusion

Photocatalysis represents a promising approach to alleviate MPs pollution in water environments. In this work, the prepared FeB/TiO_2 catalyst demonstrated excellent performance in the photocatalytic degradation of PS-MPs (92.3% particle size reduction after 12 h) and superior H_2 evolution (103.5 μmol in 12 h). The enhanced activity was due to the strong light-harvesting properties and the rapid photoelectron-hole separation after FeB modification, which promoted efficient ROS generation and accelerated the combination of photogenerated electrons with protons. In addition, the photocatalytic PS-MPs degradation reaction pathway has not been clarified previously. This report elucidates the key steps in the photodegradation of PS-MPs in aquatic environments in the presence of an FeB/TiO_2 composite. During photocatalytic PS-MPs degradation, the α-C of the benzene ring of PS-MPs was more vulnerable to deprive hydrogen by ROS, followed by subsequent chain propagation and chain termination reactions.

DFT calculations indicated that this process occurred more readily in the presence of $^{\bullet}OH$ relative to $^{\bullet}O_2^-$. Moreover, the activation energy of chain propagation decreased with the addition of FeB/TiO_2. In addition, valuable organic compounds, including benzaldehyde, phenylacetaldehyde, and benzoic acid, were detected as products, thus further supporting the possibility of photocatalytic MPs recycling. More importantly, the FeB/TiO_2 composite promoted a synergetic H_2 evolution reaction along with MPs degradation. This reactivity is promising for energy recycling while degrading pollutants in aquatic environments.

Limitations of the study

We prepared a transition metal (iron) boride/semiconductor photocatalyst (i.e., FeB/TiO_2) and investigated the performance in PS-MPs conversion and water splitting. The photocatalytic mechanism and reaction pathways for PS-MPs degradation were elucidated in this work. However, only one model MPs was investigated. Future study will include more types of MPs. Also, the photocatalytic performance will be further probed in the actual wastewater containing MPs.

STAR★METHODS

Detailed methods are provided in the online version of this paper and include the following:

- KEY RESOURCES TABLE
- RESOURCE AVAILABILITY
  - Lead contact
  - Materials availability
  - Data and code availability
- METHOD DETAILS
  - Catalysts preparation
  - Catalysts characterization
  - Photocatalytic PS-MPs degradation and H_2 evolution reaction
  - PS-MPs characterization
  - Analysis of products and reactive oxygen species
  - DFT calculations
  - Model building and calculational method
- QUANTIFICATION AND STATISTICAL ANALYSIS

SUPPLEMENTAL INFORMATION

Supplemental information can be found online at https://doi.org/10.1016/j.isci.2023.106833.

AUTHOR CONTRIBUTIONS

J.H., Conceptualization, Methodology, Formal Analysis, Investigation and Writing – Original Draft. L.H., Conceptualization, Supervision, Writing – Review & Editing, and Funding Acquisition. W.M. and L.C., Investigation and Methodology. C.M. and C.X., Formal Analysis and Writing – Review & Editing. Z.Y., Writing – Review & Editing and Project Administration.

DECLARATION OF INTERESTS

The authors declare no competing interests.

INCLUSION AND DIVERSITY

We support inclusive, diverse, and equitable conduct of research.

REFERENCES

1. Mai, L., Sun, X.F., Xia, L.L., Bao, L.J., Liu, L.Y., and Zeng, E.Y. (2020). Global riverine plastic outflows. Environ. Sci. Technol. *54*, 10049–10056.

2. Mai, L., You, S.N., He, H., Bao, L.J., Liu, L.Y., and Zeng, E.Y. (2019). Riverine microplastic pollution in the Pearl River Delta, China: are modeled estimates accurate? Environ. Sci. Technol. *53*, 11810–11817.

3. Mai, L., He, H., Bao, L.J., Liu, L.Y., and Zeng, E.Y. (2020). Plastics are an insignificant carrier of riverine organic pollutants to the coastal oceans. Environ. Sci. Technol. *54*, 15852–15860.

4. Li, L., Luo, Y., Li, R., Zhou, Q., Peijnenburg, W., Yin, N., Yang, J., Tu, C., and Zhang, Y. (2020). Effective uptake of submicrometre plastics by crop plants via a crack-entry mode. Nat. Sustain. *3*, 929–937.

5. Jiang, X., Tian, L., Ma, Y., and Ji, R. (2019). Quantifying the bioaccumulation of nanoplastics and PAHs in the clamworm Perinereis aibuhitensis. Sci. Total Environ. *655*, 591–597.

6. Ma, Y., Huang, A., Cao, S., Sun, F., Wang, L., Guo, H., and Ji, R. (2016). Effects of nanoplastics and microplastics on toxicity, bioaccumulation, and environmental fate of phenanthrene in fresh water. Environ. Pollut. *219*, 166–173.

7. Ahmad, M., Li, J.L., Wang, P.D., Hozzein, W.N., and Li, W.J. (2020). Environmental perspectives of microplastic pollution in the aquatic environment: a review. Mar. Life Sci. Technol. *2*, 414–430.

8. Cheung, P.K., and Fok, L. (2017). Characterisation of plastic microbeads in facial scrubs and their estimated emissions in Mainland China. Water Res. *122*, 53–61.

9. Mao, R., Hu, Y., Zhang, S., Wu, R., and Guo, X. (2020). Microplastics in the surface water of Wuliangsuhai Lake, northern China. Sci. Total Environ. *723*, 137820.

10. Aljaibachi, R., Laird, W.B., Stevens, F., and Callaghan, A. (2020). Impacts of polystyrene microplastics on *Daphnia magna*: a laboratory and a mesocosm study. Sci. Total Environ. *705*, 135800.

11. Mao, Y., Ai, H., Chen, Y., Zhang, Z., Zeng, P., Kang, L., Li, W., Gu, W., He, Q., and Li, H. (2018). Phytoplankton response to polystyrene microplastics: perspective from an entire growth period. Chemosphere *208*, 59–68.

12. Wang, X., Zheng, H., Zhao, J., Luo, X., Wang, Z., and Xing, B. (2020). Photodegradation elevated the toxicity of polystyrene microplastics to grouper (*Epinephelus moara*) through disrupting hepatic lipid homeostasis. Environ. Sci. Technol. *54*, 6202–6212.

13. Wang, Y., Ding, K., Ren, L., Peng, A., and Zhou, S. (2022). Biodegradable microplastics: a review on the interaction with pollutants and influence to organisms. Bull. Environ. Contam. Toxicol. *108*, 1006–1012.

14. Zhang, Y. (2021). Photodegradable and strong plastics. Nat. Sustain. *4*, 1018.

15. Ellis, L.D., Rorrer, N.A., Sullivan, K.P., Otto, M., McGeehan, J.E., Román-Leshkov, Y., Wierckx, N., and Beckham, G.T. (2021). Chemical and biological catalysis for plastics recycling and upcycling. Nat. Catal. *4*, 539–556.

16. Li, X., Chen, Y., Tao, Y., Shen, L., Xu, Z., Bian, Z., and Li, H. (2022). Challenges of photocatalysis and their coping strategies. Chem Catal. *2*, 1315–1345.

17. Bian, Z., Zhu, J., and Li, H. (2016). Solvothermal alcoholysis synthesis of hierarchical TiO₂ with enhanced activity in environmental and energy photocatalysis. J. Photoch. Photobio. C *28*, 72–86.

18. Zeng, G., You, H., Du, M., Zhang, Y., Ding, Y., Xu, C., Liu, B., Chen, B., and Pan, X. (2021). Enhancement of photocatalytic activity of TiO₂ by immobilization on activated carbon for degradation of aquatic naphthalene under sunlight irradiation. Chem. Eng. J. *412*, 128498.

19. Hwang, J.Y., Moon, G.h., Kim, B., Tachikawa, T., Majima, T., Hong, S., Cho, K., Kim, W., and Choi, W. (2021). Crystal phase-dependent generation of mobile OH radicals on TiO₂: revisiting the photocatalytic oxidation mechanism of anatase and rutile. Appl. Catal. B Environ. *286*, 119905.

20. Cao, Y., Li, X., Bian, Z., Fuhr, A., Zhang, D., and Zhu, J. (2016). Highly photocatalytic activity of brookite/rutile TiO₂ nanocrystals with semi-embedded structure. Appl. Catal. B Environ. *180*, 551–558.

21. Chen, Y., Li, H., and Bian, Z. (2021). Effect of core-shell structure of TiO₂ on its photocatalytic performance. In Core-Shell and Yolk-Shell Nanocatalysts, H. Yamashita and H. Li, eds. (Springer Singapore), pp. 443–458.

22. Kim, W., Tachikawa, T., Moon, G.h., Majima, T., and Choi, W. (2014). Molecular level understanding of the photocatalytic activity difference between anatase and rutile nanoparticles. Angew. Chem., Int. Ed. Engl. *53*, 14036–14041.

23. He, J., Lyu, P., Li, D., Cheng, C., Chang, S., Qin, L., Zheng, C., and Zhu, J. (2021). Bio-alcohol induced self-assembly of heterojunctioned TiO₂/WO₃ composites into a hierarchical yolk-shell structure for photocatalysis. Chem. Commun. (J. Chem. Soc. Sect. D) *57*, 6883–6886.

24. Ariza-Tarazona, M.C., Villarreal-Chiu, J.F., Hernández-López, J.M., Rivera De la Rosa, J., Barbieri, V., Siligardi, C., and Cedillo-González, E.I. (2020). Microplastic pollution reduction by a carbon and nitrogen-doped TiO₂: effect of pH and temperature in the photocatalytic degradation process. J. Hazard Mater. *395*, 122632.

25. Dawood, F., Anda, M., and Shafiullah, G.M. (2020). Hydrogen production for energy: an overview. Int. J. Hydrogen Energy *45*, 3847–3869.

26. Acar, C., and Dincer, I. (2019). Review and evaluation of hydrogen production options for better environment. J. Clean. Prod. *218*, 835–849.

27. Zhang, Y., Wang, C., Zhang, X., Li, H., Li, X., Lin, Y., and Park, S. (2018). Photocatalytic hydrogen evolution *via* water splitting: a short review. Catalysts *62*, 655–662.

28. Zhu, Q., Xu, Z., Qiu, B., Xing, M., and Zhang, J. (2021). Emerging cocatalysts on g-C₃N₄ for photocatalytic hydrogen evolution. Small *17*, 2101070.

29. Yang, H. (2021). A short review on heterojunction photocatalysts: carrier transfer behavior and photocatalytic mechanisms. Mater. Res. Bull. *142*, 111406.

30. Chen, D., Cheng, Y., Zhou, N., Chen, P., Wang, Y., Li, K., Huo, S., Cheng, P., Peng, P., Zhang, R., et al. (2020). Photocatalytic degradation of organic pollutants using TiO₂-based photocatalysts: a review. J. Clean. Prod. *268*, 121725.

31. Mishra, P., Patnaik, S., and Parida, K. (2019). An overview of recent progress on noble metal modified magnetic Fe₃O₄ for photocatalytic pollutant degradation and H₂ evolution. Catal. Sci. Technol. *9*, 916–941.

32. Zhu, Q., Qiu, B., Du, M., Xing, M., and Zhang, J. (2018). Nickel boride cocatalyst boosting efficient photocatalytic hydrogen evolution reaction. Ind. Eng. Chem. Res. *57*, 8125–8130.

33. Li, L., Deng, Z., Yu, L., Lin, Z., Wang, W., and Yang, G. (2016). Amorphous transitional metal borides as substitutes for Pt cocatalysts for photocatalytic water splitting. Nano Energy *27*, 103–113.

34. Song, L., Zhang, S., Liu, D., Sun, S., and Wei, J. (2020). High-performance hydrogen evolution of NiB/ZnCdS under visible light irradiation. Int. J. Hydrogen Energy 45, 8234–8242.

35. Man, Y., Shaik, F., Jiang, B., and Zheng, J. (2020). An iron-group metal boride/boron-doped vertically oriented graphene as efficient catalyst for overall water splitting in a wide pH range. J. Electrochem. Soc. 167, 122513.

36. Mahmoud, M.S., Ahmed, E., Farghali, A.A., Zaki, A.H., and Barakat, N.A. (2018). Synthesis of Fe/Co-doped titanate nanotube as redox catalyst for photon-induced water splitting. Mater. Chem. Phys. 217, 125–132.

37. Hao, W., Yao, D., Xu, Q., Wang, R., Zhang, C., Guo, Y., Sun, R., Huang, M., and Chen, Z. (2021). Highly efficient overall-water splitting enabled via grafting boron-inserted Fe-Ni solid solution nanosheets onto unconventional skeleton. Appl. Catal. B Environ. 292, 120188.

38. Humayun, M., Xu, L., Zhou, L., Zheng, Z., Fu, Q., and Luo, W. (2018). Exceptional co-catalyst free photocatalytic activities of B and Fe co-doped SrTiO3 for CO2 conversion and H2 evolution. Nano Res. 11, 6391–6404.

39. Uekert, T., Kasap, H., and Reisner, E. (2019). Photoreforming of nonrecyclable plastic waste over a carbon nitride/nickel phosphide catalyst. J. Am. Chem. Soc. 141, 15201–15210.

40. Cao, B., Wan, S., Wang, Y., Guo, H., Ou, M., and Zhong, Q. (2022). Highly-efficient visible-light-driven photocatalytic H2 evolution integrated with microplastic degradation over MXene/ZnxCd1-xS photocatalyst. J. Colloid Interface Sci. 605, 311–319.

41. Wang, Z., Chen, Y., Zhang, L., Cheng, B., Yu, J., and Fan, J. (2020). Step-scheme CdS/TiO2 nanocomposite hollow microsphere with enhanced photocatalytic CO2 reduction activity. J. Mater. Sci. Technol. 56, 143–150.

42. Wang, L., Cheng, B., Zhang, L., and Yu, J. (2021). In situ irradiated xps investigation on s-scheme TiO2@ZnIn2S4 photocatalyst for efficient photocatalytic CO2 reduction. Small 17, 2103447.

43. Flak, D., Chen, Q., Mun, B.S., Liu, Z., Rękas, M., and Braun, A. (2018). In situ ambient pressure XPS observation of surface chemistry and electronic structure of α-Fe2O3 and γ-Fe2O3 nanoparticles. Appl. Surf. Sci. 455, 1019–1028.

44. Shen, W., Mu, Y., Xiao, T., and Ai, Z. (2016). Magnetic Fe3O4-FeB nanocomposites with promoted Cr(VI) removal performance. Chem. Eng. J. 285, 57–68.

45. Choudhury, B., and Choudhury, A. (2013). Tailoring luminescence properties of TiO2 nanoparticles by Mn doping. J. Lumin. 136, 339–346.

46. An, Y., Liu, Y., An, P., Dong, J., Xu, B., Dai, Y., Qin, X., Zhang, X., Whangbo, M.H., and Huang, B. (2017). NiII coordination to an Al-based metal-organic framework made from 2-aminoterephthalate for photocatalytic overall water splitting. Angew. Chem. 129, 3082–3086.

47. Liang, Z., Bai, X., Hao, P., Guo, Y., Xue, Y., Tian, J., and Cui, H. (2019). Full solar spectrum photocatalytic oxygen evolution by carbon-coated TiO2 hierarchical nanotubes. Appl. Catal. B Environ. 243, 711–720.

48. Uheida, A., Mejía, H.G., Abdel-Rehim, M., Hamd, W., and Dutta, J. (2021). Visible light photocatalytic degradation of polypropylene microplastics in a continuous water flow system. J. Hazard Mater. 406, 124299.

49. Jiang, R., Lu, G., Yan, Z., Liu, J., Wu, D., and Wang, Y. (2021). Microplastic degradation by hydroxy-rich bismuth oxychloride. J. Hazard Mater. 405, 124247.

50. Fakhri, L.A., Ghanbarzadeh, B., Dehghannya, J., Hosseini, M., and Dadashi, S. (2021). Photo-catalytic and biotic degradation of polystyrene packaging film: effect of zinc oxide photocatalyst nanoparticles and nanoclay. Chemosphere 283, 130972.

51. Kumar, A., Jangir, L.K., Kumari, Y., Kumar, M., Kumar, V., and Awasthi, K. (2015). Optical and structural study of polyaniline/polystyrene composite films. Macromol. Symp. 357, 229–234.

52. Chen, G., Liu, S., Chen, S., and Qi, Z. (2001). FTIR spectra, thermal properties, and dispersibility of a polystyrene/montmorillonite nanocomposite. Macromol. Chem. Phys. 202, 1189–1193.

53. Zan, L., Wang, S., Fa, W., Hu, Y., Tian, L., and Deng, K. (2006). Solid-phase photocatalytic degradation of polystyrene with modified nano-TiO2 catalyst. Polymer 47, 8155–8162.

54. Yousif, E., and Haddad, R. (2013). Photodegradation and photostabilization of polymers, especially polystyrene: review. SpringerPlus 2, 398.

55. Llorente-García, B.E., Hernández-López, J.M., Zaldívar-Cadena, A.A., Siligardi, C., and Cedillo-González, E.I. (2020). First insights into photocatalytic degradation of HDPE and LDPE microplastics by a mesoporous N-TiO2 coating: effect of size and shape of microplastics. Coatings 10, 658.

56. Mylläri, V., Ruoko, T.P., and Syrjälä, S. (2015). A comparison of rheology and FTIR in the study of polypropylene and polystyrene photodegradation. J. Appl. Polym. Sci. 132, 42246.

57. Yu, H., Zhang, L., Zang, J., Xiao, L., and Luo, J. (2020). Triethanolamine-mediated photodeposition formation of amorphous Ni-P alloy for improved H2-evolution activity of g-C3N4. Sci. China Mater. 5, 2215–2216.

58. He, J., Lyu, P., Jiang, B., Chang, S., Du, H., Zhu, J., and Li, H. (2021). A novel amorphous alloy photocatalyst (NiB/In2O3) composite for sunlight-induced CO2 hydrogenation to HCOOH. Appl. Catal. B Environ. 298, 120603.

59. Nosaka, Y., and Nosaka, A.Y. (2017). Generation and detection of reactive oxygen species in photocatalysis. Chem. Rev. 117, 11302–11336.

60. Xu, X., Wang, J., Chen, T., Yang, N., Wang, S., Ding, X., and Chen, H. (2021). Deep insight into ROS mediated direct and hydroxylated dichlorination process for efficient photocatalytic sodium pentachlorophenate mineralization. Appl. Catal. B Environ. 296, 120352.

61. Wei, Z., Liu, J., and Shangguan, W. (2020). A review on photocatalysis in antibiotic wastewater: pollutant degradation and hydrogen production. Chin. J. Catal. 41, 1440–1450.

62. Hussain, T., Hussain, M., Hussain, S., and Kaseem, M. (2022). Microwave-assisted synthesis of NiTe2 photocatalyst as a facile and scalable approach for energy-efficient photocatalysis and detoxification of harmful organic dyes. Sep. Purif. Technol. 282, 120025.

63. Parrino, F., Livraghi, S., Giamello, E., Ceccato, R., and Palmisano, L. (2020). Role of hydroxyl, superoxide, and nitrate radicals on the fate of bromide ions in photocatalytic TiO2 suspensions. ACS Catal. 10, 7922–7931.

64. Liu, Z., Lv, Y., Wang, Y., Wang, S., Odebiyi, O.S., Liu, B., Zhang, Y., and Du, H. (2022). Oxidative leaching of V-Cr–bearing reducing slag via a Cr(III) induced Fenton-like reaction in concentrated alkaline solutions. J. Hazard Mater. 439, 129495.

65. Aljabri, N.M., Lai, Z., Hadjichristidis, N., and Huang, K.W. (2017). Renewable aromatics from the degradation of polystyrene under mild conditions. J. Saudi Chem. Soc. 21, 983–989.

66. Sarwan, B., Acharya, A.D., Kaur, S., and Pare, B. (2020). Visible light photocatalytic deterioration of polystyrene plastic using supported BiOCl nanoflower and nanodisk. Eur. Polym. J. 134, 109793.

67. Maydanova, I.O., Lakeev, S.N., Ishalina, O.V., and Nikitina, A.P. (2020). Synthesis of a new benzoate plasticizer for polyvinyl chloride based on a 2-ethylhexanol by-product. Russ. J. Appl. Chem. 93, 1883–1887.

68. Yang, Y.H., Zhao, J., and Du, Z.Z. (2022). Unravelling the key aroma compounds in the characteristic fragrance of dendrobium officinale flowers for potential industrial application. Phytochemistry 200, 113223.

69. Wang, H.J., Lin, H.H.H., Hsieh, M.C., and Lin, A.Y.C. (2022). Photoaged polystyrene microplastics serve as photosensitizers that enhance cimetidine photolysis in an aqueous environment. Chemosphere 290, 133352.

70. Ding, L., Yu, X., Guo, X., Zhang, Y., Ouyang, Z., Liu, P., Zhang, C., Wang, T., Jia, H., and Zhu, L. (2022). The photodegradation processes and mechanisms of polyvinyl chloride and polyethylene terephthalate microplastic in aquatic environments: important role of clay minerals. Water Res. 208, 117879.

71. Wu, X., Liu, P., Wang, H., Huang, H., Shi, Y., Yang, C., and Gao, S. (2021). Photo aging of

polypropylene microplastics in estuary water and coastal seawater: important role of chlorine ion. Water Res. *202*, 117396.

72. Chi, Y., Wang, W., Zhang, Q., Yu, H., Liu, M., Ni, S., Gao, B., and Xu, S. (2021). Evaluation of practical application potential of a photocatalyst: ultimate apparent photocatalytic activity. Chemosphere *285*, 131323.

73. Zhang, Y., Cao, H., Lu, J., Li, Y., and Bao, M. (2022). Enhanced photocatalytic activity of glyphosate over a combination strategy of GQDs/TNAs heterojunction composites. J. Colloid Interface Sci. *607*, 607–620.

74. Ma, H.Y., Zhao, L., Guo, L.H., Zhang, H., Chen, F.J., and Yu, W.C. (2019). Roles of reactive oxygen species (ROS) in the photocatalytic

degradation of pentachlorophenol and its main toxic intermediates by TiO_2/UV. J. Hazard Mater. *369*, 719–726.

75. Xu, L., Li, H., Mitch, W.A., Tao, S., and Zhu, D. (2019). Enhanced phototransformation of tetracycline at smectite clay surfaces under simulated sunlight via a lewis-base catalyzed alkalization mechanism. Environ. Sci. Technol. *53*, 710–718.

STAR★METHODS

KEY RESOURCES TABLE

REAGENT or RESOURCE	SOURCE	IDENTIFIER
Chemicals, peptides, and recombinant proteins		
Glycerol	Aladdin	CAS 56-81-5
Ethanol	Aladdin	CAS 64-17-5
Ether	Guangzhou	CAS 100-41-4
Titanyl sulfate	Sigma-aldrich	CAS 13825-75-6
Sodium hydroxide	Aladdin	CAS 1310-73-2
Sodium borohydride	Aladdin	CAS 16940-66-2
Ferrous sulfate	Aladdin	CAS 7720-78-7
Critical commercial assays		
Multi-channel photocatalytic reactor	Beijing Perfect Light	PCX-50C
Software and algorithms		
Density functional theory	Materials Studio	BIOVIA, USA
OriginPro 2019	OriginLab Corporation	Massachusetts, USA
Other		
Optical microscope	Olympus	CKX53
Fourier transform infrared spectroscopy	Shimadzu	IRTracer-100
Gas chromatograph	Thermo Fisher Scientific	TRACE 1300
Gas chromatography-mass spectrometry	Agilent	GCMS-7890
Electron paramagnetic resonance	Bruker	EMXplus
Inductively coupled plasma mass spectrometry	Thermo Fisher Scientific	iCAP™ RQ
X-ray diffraction	Bruker	Bruker D8 Advance
Field emission scanning electronic microscopy	JEOL	JSM-6380LV
Transmission electronic microscopy	Talos	Talos F200X G2, superX
X-ray photoelectron spectroscopy	Thermo Fisher Scientific	K-Alpha Nexsa using Al Kα radiation
UV-vis diffuse reflection spectra	Shimadzu	UV-2450
Steady-state photoluminescence	HORIBA	Fluorolog-3

RESOURCE AVAILABILITY

Lead contact

Further information and requests for resources and reagents should be directed to and will be fulfilled by the Lead Contact, Professor Lanfang Han (hanlanfang@gdut.edu.cn)

Materials availability

This study did not generate new unique reagent.

Data and code availability

- The published article includes all datasets generated or analyzed during this study.

- Any additional information required to reanalyze the data reported in this paper is available from the lead contact upon request.

- This paper does not report original code.

METHOD DETAILS

Catalysts preparation

The core-shell structured TiO_2 was prepared using a modified alcoholysis method reported in our previous work.[23] Briefly, 10 mL of glycerol (Aladdin, AR) and 20 mL of ethanol (EtOH; Aladdin, AR) were mixed at $25 \pm 0.5\,°C$, and then 10 mL of ether (Guangzhou, AR) were added dropwise into the solution. After stirring for 10 min, 1 mL of $TiOSO_4$ (Sigma-aldrich, ~15 wt % in dilute sulfuric acid) was carefully dropped into the solution and the mixture was stirred for 30 min. The resulting solution was transferred to a 50 mL Teflon-lined stainless-steel kettle and placed into an oven at 110 °C for 48 h. The precipitate was centrifuged, washed with EtOH, and dried at 60 °C for 12 h. The sample was then calcined at 550 °C in air for 3 h, and the obtained TiO_2 with core-shell structure was donated as CST.

Amorphous FeB was synthesized via chemical reduction. Briefly, an aqueous solution of $NaBH_4/NaOH$ (2 M/0.2 M) (Aladdin, AR) was added dropwise into an $FeSO_4$ solution (0.85 M) (Aladdin, AR) at an ice bath under vigorous stirring under a N_2 atmosphere. The solution was stirred continuously for approximately 0.5 h until no more bubbles were released. Excess $NaBH_4$ was used to ensure the complete reduction of Fe ions. The black precipitate was washed thoroughly with ultrapure water to remove soluble boron species and Na^+ ions. Finally, the samples were washed with EtOH and stored in EtOH until further use.

The FeB/TiO_2 composites were prepared as follows. First, 100 mg of CST was impregnated with an $FeSO_4$ solution (0.85 M) overnight. The suspension was then dried at 60 °C and calcined at 200 °C for 2 h. Subsequently, it was dispersed into 10 mL of ultrapure water, and an aqueous $NaBH_4/NaOH$ (2 M/0.2 M) solution was added dropwise while the reaction vessel was cooled in an ice bath and stirred vigorously under a N_2 atmosphere. The sample was then washed thoroughly with water and EtOH. The prepared samples were labeled as xFBT, where x is the theoretical mass ratio of Fe deposited onto the TiO_2; this ratio was adjusted based on the added $FeSO_4$ solution. As a comparison, commercial TiO_2 without core-shell structure was introduced instead of CST, and the FeB amount was same with 7FBT, which was named as 7FBT-Commercial.

Catalysts characterization

The FeB content in all composite was determined using inductively coupled plasma mass spectrometry (ICP-MS, Thermo Fisher Scientific, iCAP RQ) (Table S1). The N_2 adsorption -desorption isotherms were obtained at 77 K with a micromeritics ASAP 2010 instrument, which allowed calculations of the specific surface area (S_{BET}), pore size (D_P), and pore volume (V_P) by applying Brunauer-Emmett-Teller (BET) and Barrett-Joyner-Halenda (BJH) models. The crystal structure was determined by X-ray diffraction (XRD) using a Bruker D8 Advance X-ray diffractometer with Cu-Kα radiation at a scanning rate of 5°/min. The morphologies and particle sizes were observed using field emission scanning electronic microscopy (FESEM; JEOL JSM-6380LV) and transmission electronic microscopy (TEM; Talos F200X G2, superX). The elemental distribution was obtained using energy-dispersive X-ray spectroscopy (EDS). The surface electronic states were investigated by X-ray photoelectron spectroscopy (XPS; Thermo Scientific K-Alpha Nexsa using Al Kα radiation). The light-absorbance was measured by UV-vis diffuse reflection spectra (DRS) on a Shimadzu UV-2450 Spectrophotometer with $BaSO_4$ as a reference. The steady-state photoluminescence (PL) and transient fluorescence spectra (TRPL) were obtained using a HORIBA Fluorolog-3 fluorometer at an excitation wavelength of 350 nm. Photocurrent and electrochemical impedance spectra were obtained using an electrochemical analyzer (CHI760D Instruments) with a standard three-electrode system, where a 0.5 M Na_2SO_4 aqueous solution was used as the electrolyte. For photocurrent test, the system was irradiated with a 300 W Xe lamp at an interval of 30 s. With respect to EIS measurement, the high and low frequency was set to 10^5 Hz and 10 mHz. For electrochemical characterizations, the sample was prepared according to previously reported procedures.[58] Specifically, a working electrode containing catalyst was prepared as follow: 2 mg polyvinylidene fluoride was dissolved in 2 mL dimethyl formamide solution under ultrasonic condition. Then, 20 mg as-prepared catalyst was added. The suspension was treated by ultrasound for another 5 min, followed by dropping onto an F-doped SnO_2 transparent conductive glass piece (20 × 20 mm²), vacuum drying at 80 °C for 8 h, and calcination at 150 °C for 1 h. A Pt piece with an area of 20 × 20 mm² was used as a counter electrode and a saturated calomel electrode was used as a reference electrode.

Photocatalytic PS-MPs degradation and H$_2$ evolution reaction

The PS-MPs (diameter: ~200 μm; density: 1.05 g/cm^3) were purchased from Guangzhou Huayu Environmental Technology, Inc. (Guangzhou, China). They were washed with ultrapure water several times and filtered through a cotton filter to remove chemicals that may be adsorbed on the PS-MPs surface. Then, the filtered ones were freeze-dried for 24 h. The photocatalytic MPs degradation was carried out in a PCX-50C Discover multi-channel photocatalytic reactor (Beijing Perfect Light Technology Co., Ltd., China) equipped with a 365 nm LED (5 W) lamp as the light source since UV radiation is considered one of the primary factors in MPs photodegradation in natural environment.[69,70] The reactor comprised a 50 mL sealed glass vial with a quartz bottom, as shown in Figure S1. Before the reaction, 30 mg of PS and 50 mg of the prepared photocatalyst were added to 30 mL of ultrapure water and sonicated for 5 min. Then, the light was turned on to initiate the reaction, and the reaction temperature was controlled at 25 °C with a circulating water bath. The gas products were sampled, and the MPs remaining after reaction were collected with a 10 μm filter to separate them. Then, they were washed four times with ultrapure water, freeze-dried, and stored in the dark for further analysis. The PS-MPs photodegradation was also performed without a catalyst and under dark conditions as control experiments.

PS-MPs characterization

The particle sizes of the PS-MPs were examined using an optical microscope (Olympus CKX53, Japan). Fourier transform infrared spectroscopy (FTIR; Shimadzu IRTracer-100, Japan) was used to explore the surface functional groups of the original and photodegraded PS-MPs. The FTIR spectral range was from 4000 to 400 cm^{-1}, and each spectrum adopted the average of 32 scans with 4 cm^{-1} resolution. The carbonyl index (CI) is calculated by the ratio of the area of the carbonyl absorption band (1870-1540 cm^{-1}) to the area of the reference absorption band (2851 cm^{-1}), which corresponds to the symmetric stretching band of CH$_2$ moieties in the PS-MPs.[56]

Analysis of products and reactive oxygen species

The H$_2$ production and CO$_2$ accumulation were measured using a gas chromatograph (GC; Thermo Scientific, TRACE 1300, America) equipped with a thermal conductivity detector and a PORAPAK packed column using Ar as the carrier gas. The reaction intermediates were filtered, extracted with methanol, and then analyzed by gas chromatography-mass spectrometry (GCMS; Agilent, GCMS-7890, America) using an HP-5MS column; the compounds were identified based on the MS database provided by the National Institute of Standards and Technology (NIST). The formation of ·OH and ·O$_2^-$ (i.e., ROS) during the reaction was analyzed using electron paramagnetic resonance (EPR) spectroscopy (Bruker EMXplus, Germany) using 5,5-dimethyl-1-pyrroline N-oxide (DMPO; 50 mM) to capture ·OH and ·O$_2^-$.[71] The instrumental parameters were set as follows: center field = 3510 G; microwave frequency = 9.853 GHz; microwave power = 20 mW. The dark control experiment was conducted under the same conditions without light irradiation. The radical quenching experiment was conducted to evaluate the contribution of different radicals in the reaction. The scavengers, including tertiary butyl alcohol (TBA; 10 mM), 4-benzoquinone (10 mM), ethylenediaminetetraacetic acid disodium salt (EDTA-2Na; 10 mM), and 2,3-dichloro-5,6-dicyano-1,4-benzoquinone (DDQ; 10 mM), were used to capture the ·OH, ·O$_2^-$, holes, and electrons, respectively.[72–74] The average particle size reduction of PS-MPs and the H$_2$ production (with radical scavenging) were analyzed after 8 h of irradiation.

·OH concentration was quantified by terephthalic acid (TPA) probe method (Figure S12).[64] Specifically, 0.5 mM TPA was dissolved in 2 mM NaOH solution and filtered through a 0.45 μm filter (Nylon). Then, 50 mg of photocatalyst was added to 50 mL reaction solution. TPA was combined with ·OH to form hydroxy terephthalic acid (HTPA). After reaction, the reaction solution was sampled and detected with a fluorescence spectrophotometer. The excitation and emission wavelengths were set at 315 nm and 425 nm, respectively.[75] [·OH] was calculated as follows and the results was displayed in Table S5.

$$[OH] = f(0.01127FI - 0.26137)$$

Where f is the trapping factor, and f = 1.25; FI is fluorescence intensity; [OH]$_{ss}$ is the steady concentration of ·OH (μM).

DFT calculations

All self-consistent periodic DFT calculations were carried out using the DMol[3] code, as implemented in the Materials Studio package. The electron exchange and correlation were described with a Generalized gradient approximation-Perdew Burke Ernzerhof (GGA-PBE) functional. The localized double-numerical quality basis set with a polarization d-function (DNP-4.4 file) was used to expand the wave functions. To accommodate the van der Waals interactions in the DFT calculations, the Grimme-06 (DFT-D) method was used for dispersion corrections. The core electrons of the metal atoms were treated using the effective core potentials (ECP), and the orbital cutoff was 4.5 Å for all atoms. For geometry optimizations, the convergences of the energy, maximum force, and maximum displacement were set as 2×10^{-5} Ha, 4×10^{-3} Ha/Å, and 5×10^{-3} Å, respectively, and the self-consistent field (SCF) convergence for each electronic energy level was set as 1.0×10^{-5} Ha. The Brillouin-zone integrations were sampled using the Γ Monkhorst-Pack mesh for geometry optimizations. The transition states (TS) of the elementary steps were determined at the same theoretical level using the complete linear synchronous transit/quadratic synchronous transit (LST/QST) approach.

Model building and calculational method

The calculation model uses of anatase TiO_2 (101) crystal plane, and the supercell is (3 × 4× 1). The bottom three atomic layers are fixed, the others four atomic layers are kept free, and the vacuum layer is set 15 Å to consider to make sure that the slab is isolated in the Z-direction. All the self-consistent periodic DFT calculations were carried out using the DMol[3] code as implemented in the Materials Studio package. The electron exchange and correlation were described with GGA-PBE functional. The localized double-numerical quality basis set with a polarization d-function (DNP-4.4 file) was chosen to expand the wave functions. To accommodate the van der Waals interactions, the Grimme-06 (DFT-D) method was used for dispersion correction in the DFT calculations. The core electrons of the metal atoms were treated using the effective core potentials (ECP), and the orbital cutoff was 4.5 Å for all atoms. For the geometry optimization, the convergences of the energy, maximum force, and maximum displacement were set as 2×10^{-5} Ha, 4×10^{-3} Ha/Å, and 5×10^{-3} Å, and the SCF convergence for each electronic energy was set as 1.0×10^{-5} Ha. The Brillouin-zone integrations were sampled by using the Γ Monkhorst-Pack mesh for geometry optimization. The transition states (TSs) of the elementary steps were performed at the same theoretical level using the complete linear synchronous transit and quadratic synchronous transit (LST/QST) approach. The original data of the activation energy of transition states were provided in Table S6.

QUANTIFICATION AND STATISTICAL ANALYSIS

All the results were the average of tri-measurements with standard error.